Chinese Chemical Letters 37 (2026) 111866

Contents lists available at ScienceDirect

Chinese Chemical Letters

journal homepage: www.elsevier.com/locate/cclet

Novel 2D/1D MXene/Bi_5O_7I Schottky junction for photocatalytic degradation of bisphenol AF by peroxymonosulfate-assisted photocatalysis

Feihu Mu[a], Benlin Dai[a], Chuxuan Dai[a], Xiaozhong Chu[a], Jiming Xu[a], Junyu Shen[b,*], Wei Zhao[b,*], Guohui Dong[c,*]

[a] Jiangsu Key Laboratory for Chemistry of Low-Dimensional Materials, School of Chemistry and Chemical Engineering, Huaiyin Normal University, Huaian 223300, China
[b] School of Materials Engineering, Suzhou University of Technology, Changshu 215500, China
[c] School of Environmental Science and Engineering, Shaanxi University of Science & Technology, Xi'an 710021, China

ARTICLE INFO

Article history:
Received 22 May 2025
Revised 7 August 2025
Accepted 21 September 2025
Available online 22 September 2025

Keywords:
MXene
Schottky junction
Peroxymonosulfate
Photocatalysis
PMS

ABSTRACT

Considering the urgency of endocrine disrupting chemicals (EDCs) management, a novel 2D MXene/1D Bi_5O_7I Schottky junction photocatalyst was constructed for the degradation of bisphenol AF (BPAF) by peroxymonosulfate (PMS)-assisted photocatalytic system. Under visible light, the 8-MXene/Bi_5O_7I/PMS system could degrade 93.4% (0.02984 min^{-1}) of BPAF at 90 min, which was 5.04 and 3.35 times that of Bi_5O_7I and MXene/Bi_5O_7I, respectively. This demonstrated the synergistic interaction between photocatalysis and PMS activation, and the ability of MXene to promote the reaction. Density functional theory (DFT) calculations combined with experiments revealed the catalytic reaction mechanism of the system. Additionally, based on Gaussian calculations, the key intermediates of the degradation process were proposed. This study provides a new insight into PMS-assisted photocatalytic systems for effective degradation of organic pollutants.

© 2026 Published by Elsevier B.V. on behalf of Chinese Chemical Society and Institute of Materia Medica, Chinese Academy of Medical Sciences.

Endocrine-disrupting chemicals (EDCs) are emerging contaminants that can affect the endocrine systems of humans and animals, harming organisms and their offspring [1,2]. Bisphenol AF (BPAF) is an analog of BPA, which has been widely adopted in many fields such as fluororubber and food processing. Concentrations of BPAF in wastewater treatment plants are as high as 16.5 ng/L [3]. Noticeably, BPAF is an EDC with higher estrogenic activity and developmental toxicity than BPA [4]. Consequently, the development of effective treatment methods for removing BPAF is a worthwhile pursuit.

So far, some studies have been published on the removal of BPAF from water using various technologies, but the results are not satisfactory. Advanced oxidation processes (AOPs), particularly sulfate radical-based AOPs, have become an effective technology for organic pollutants degradation in water bodies due to their long half-life (30–40 μs) and high redox potential [5,6]. Moreover, as an environmentally friendly technology, photocatalysis is considered a promising method for EDC elimination due to its high degradation efficiency and low cost [7,8]. Research has shown that peroxymonosulfate (PMS) can serve as an electron acceptor to inhibit photogenerated carrier recombination during photocatalysis, resulting in more reactive oxidants (ROS) [9,10]. Therefore, designing rational photocatalysts to construct PMS-assisted photocatalytic systems has attracted much attention.

Bismuth-based photocatalysts have superior photocatalytic properties due to their valence band composed of the hybridization of O 2p and Bi 6s [11,12]. In particular, as an oxygen-enriched BiOX material, Bi_5O_7I has been extensively applied in many fields. However, the weak photoresponse and slow charge transfer of pristine Bi_5O_7I hinder its photocatalytic activity. To overcome these shortcomings, some methods have been explored. Among them, the most widely adopted method is to introduce heterojunctions to form Bi_5O_7I hybrids, including g-C_3N_4/Bi_5O_7I [13], Ag_2O/Bi_5O_7I [14], and BiOI/Bi_5O_7I [15]. MXenes, a new type of 2D metal carbides, have attracted increasing attention since 2011 [16,17]. Pris-

* Corresponding authors.
E-mail addresses: shenjunyu2014@126.com (J. Shen), lmjzhaowei@foxmail.com (W. Zhao), dongguohui@sust.edu.cn (G. Dong).

https://doi.org/10.1016/j.cclet.2025.111866
1001-8417/© 2026 Published by Elsevier B.V. on behalf of Chinese Chemical Society and Institute of Materia Medica, Chinese Academy of Medical Sciences.

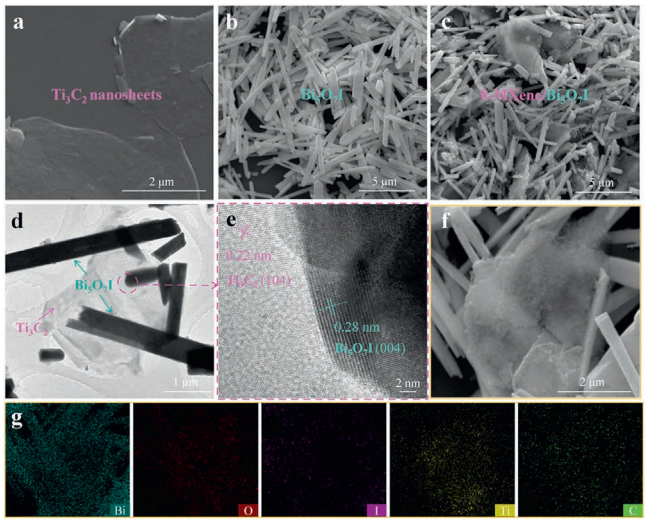


Fig. 1. FESEM images of (a) MXene nanosheets, (b) Bi_5O_7I nanorods, (c) 8-MXene/Bi_5O_7I. (d) TEM image, (e) HRTEM image, and (f, g) elemental mapping of 8-MXene/Bi_5O_7I.

tine MXenes have submetallic characteristics and can generate Schottky junctions when combined with semiconductors [18]. The Schottky barrier not only inhibits electron and hole recombination in the semiconductor but also limits electron backflow from the metal to the semiconductor [19].

Inspired by the above studies, a novel 2D MXene(Ti_3C_2)/1D Bi_5O_7I Schottky junction was constructed by a hydrothermal method and activated with PMS to degrade BPAF under visible light. Please see the Supporting Information for details on synthesis, characterization, photocatalytic activity experiments, and DFT calculations.

The construction of the 2D MXene/1D Bi_5O_7I Schottky junction consisted of two steps (Fig. S1 in Supporting information). A series of MXene/Bi_5O_7I Schottky junctions containing different mass ratios of MXene to Bi_5O_7I were obtained by adjusting the preparation conditions, as shown in Figs. S2a–d (Supporting information).

The field emission scanning electron microscopy (FESEM) (Fig. 1a) image fully demonstrates the laminar structure of MXene. The microscopic morphology of Bi_5O_7I (Fig. 1b) and 8-MXene/Bi_5O_7I (Fig. 1c) is observed by FESEM, indicating that Bi_5O_7I rods of ~5 μm in length are adhered to the surface of 2D MXene. Moreover, the transmission electron microscope (TEM) image (Fig. 1d) clearly shows the formation of a 2D/1D microstructure in MXene/Bi_5O_7I, and a clear boundary between the two materials is observed, suggesting that the Bi_5O_7I rods tightly adhere to the MXene to fabricate this 2D/1D microstructure. The HR-TEM image (Fig. 1e) shows two lattices with spacings of 0.22 and 0.28 nm, representing the MXene (104) and Bi_5O_7I (004) crystal planes, respectively. The obvious heterojunction boundary and the coexistence of the two lattices in MXene/Bi_5O_7I reveal that a heterojunction with a tight interface and strong adhesion is generated, favoring carrier migration and transfer. Elemental mapping (Figs. 1f and g) also confirms this result. The homogeneous distribution of elements Bi, O, I, Ti, and C in MXene/Bi_5O_7I indicates that the two materials are tightly bound. Obviously, a 2D/1D MXene/Bi_5O_7I junction has been successfully prepared.

Nitrogen adsorption-desorption isotherm tests (Fig. S3a in Supporting information) show that all adsorption isotherms are of type IV, suggesting the presence of mesopores [20]. From Fig. S3b and Table S1 (Supporting information), the pore sizes of the samples are 2–4 nm. Compared with the pristine Bi_5O_7I, the larger BET surface area, pore size, and pore volume of the MXene/Bi_5O_7I heterojunction can offer increased active sites, thereby enhancing the mass transfer and catalytic performance of the system.

The X-ray diffraction (XRD) pattern (Fig. S4 in Supporting information) shows that the MAX phase exhibits strong diffraction peaks, consistent with the Ti_3AlC_2 crystal (JCPDS No. 52-0875). After etching, the diffraction peaks of (002) and (004) are shifted to a lower angle, and the strongest diffraction peak of (104) at 39.0° disappears, demonstrating that the Al element is removed from Ti_3AlC_2. In Fig. S3c, the diffraction peaks of Bi_5O_7I match the standard card for Bi_5O_7I (JCPDS no 40-0583) [21]. The intensity of all the MXene/Bi_5O_7I junction diffraction peaks is weakened, probably because the growth of Bi_5O_7I crystals is inhibited by the growth-limiting effect of MXene [22]. In the FT-IR spectra (Fig. S3d), no distinct peaks are observed in MXene, and the peaks in the MXene/Bi_5O_7I junctions are similar to those of Bi_5O_7I. These XRD and FTIR tests further confirm the successfully synthesized MXene/Bi_5O_7I junction.

In X-ray photoelectron spectroscopy (XPS) survey spectra (Fig. S5a in Supporting information), 8-MXene/Bi_5O_7I contains all elements in Bi_5O_7I and MXene. In C 1s spectra (Fig. S5b in Supporting information), the peak at 286.2 eV in 8-MXene/Bi_5O_7I corresponds to C–O originating from adsorbed organic matter [22]. Meanwhile, the XPS peak at 281.6 eV belongs to C-Ti. Both C-Ti and C–O binding energies of 8-MXene/Bi_5O_7I show a 0.2 eV decrease compared with MXene. Similarly, in the Ti 2p spectra (Fig. S5c in Supporting information), the Ti-C (455.0 and 460.8 eV) and Ti-O (458.5 and 464.3 eV) binding energies of 8-MXene/Bi_5O_7I are both negatively shifted by 0.3 eV compared with MXene. Conversely, the Bi 4f spectra (Fig. S5d in Supporting information) of 8-MXene/Bi_5O_7I and MXene exhibit opposite trends. Additionally, the O 1s (Fig. S5e in Supporting information) and I 3d (Fig. S5f in Supporting information) spectra of 8-MXene/Bi_5O_7I display a similar trend with positive shifts of 0.3 and 0.2 eV, respectively.

Another piece of information obtained from XPS spectra is the internal electric field (IEF). The binding energies of all Ti elements in the MXene/Bi_5O_7I heterojunction display negative migration compared with MXene. Meanwhile, the MXene/Bi_5O_7I heterojunction exhibits higher binding energies for Bi, O, and I than Bi_5O_7I, demonstrating a decrease of electrons on Bi_5O_7I in the MXene/Bi_5O_7I heterojunction. Therefore, when the two materials are coupled to each other to form a heterojunction, electrons are transferred from Bi_5O_7I to MXene to form an electron-withdrawal layer, *i.e.*, (-) MXene/(+) Bi_5O_7I - IEF.

To further investigate the IEF, the average potential was obtained according to density-functional theory (DFT). In Figs. 2a and b, the work function (Φ) of MXene and Bi_5O_7I is 5.48 and 4.98 eV, respectively. MXene shows a larger Φ and lower Fermi energy level (E_{Fermi}) than Bi_5O_7I, implying the electrons in Bi_5O_7I are more likely to escape. When they contact each other, the electrons in Bi_5O_7I tend to transfer to MXene, while the energy band of Bi_5O_7I produces an upward bending to form a Schottky barrier (Fig. 2c) [23]. The Schottky barrier from the Schottky junction inhibits the photogenerated electron-hole complexation.

The density of states (DOS) is calculated for MXene and Bi_5O_7I, respectively. MXene (Fig. 2d) exhibits a continuum of electronic states throughout the energy levels, highlighting its excellent conductivity and confirming its submetallic nature. In the DOS of Bi_5O_7I (Fig. 2e), the highest part of the valence band consists mainly of O 2p, I 5p, and Bi 6p orbitals. In Fig. 2f, the simulated isosurfaces with different charge densities indicate that the electron migration between MXene and Bi_5O_7I leads to a strong coupling at the heterojunction interface. Further, MXene shows a negative charge at the heterojunction interface, while Bi_5O_7I is positively charged, corresponding to the XPS tests.

Figs. 3a and b show that Bi_5O_7I can respond efficiently to visible light and degrade 41.9 % of BPAF at 90 min with a

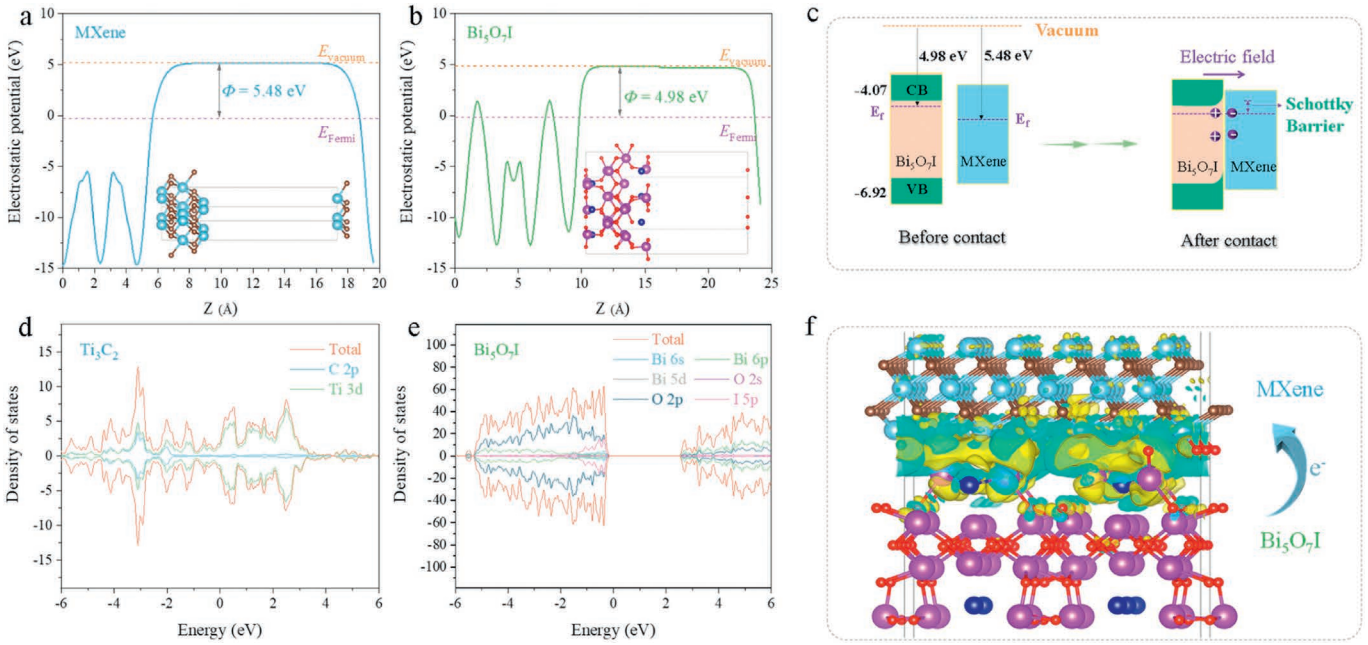


Fig. 2. Average potential profile along the Z-axis direction for (a) MXene and (b) Bi_5O_7I. (c) Schematic illustration of the Schottky junction on the interface between MXene and Bi_5O_7I. Calculated density of states (DOS) for (d) MXene and (e) Bi_5O_7I. (f) Electron density distribution in the interface between MXene and Bi_5O_7I.

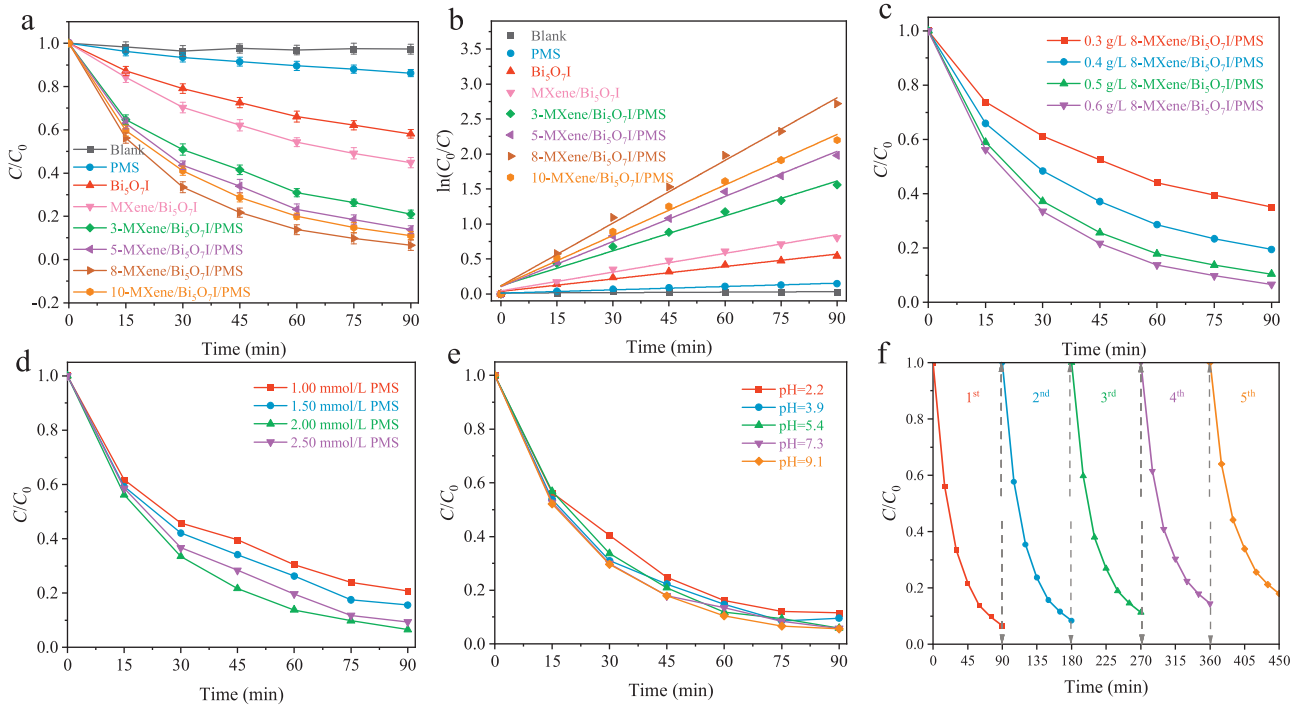


Fig. 3. (a) Photodegradation curves of BPAF, (b) *pseudo*-first-order kinetics fitted curves. Effect of catalyst dosage (c), PMS concentration (d), and pH (e) on the removal of BPAF. Conditions: Conditions: [BPAF] = 20 mg/L, [PMS] = 2.00 mmol/L, [catalyst] = 0.6 g/L, pH = 5.4, unless otherwise specified. (f) Cycle degradation experiment.

k_{app} of 0.00592 min^{-1}. After compounding MXene, the degradation rate of BPAF by MXene/Bi_5O_7I Schottky heterojunction is increased to 55.2 % (k_{app} = 0.00891 min^{-1}). Moreover, in the 3-MXene/Bi_5O_7I/PMS system, about 79.0 % of BPAF is degraded within 90 min (k_{app} = 0.01662 min^{-1}). The performance of the MXene/Bi_5O_7I/PMS system in degrading BPAF increases further with the increase of MXene content. Among them, 8-MXene/Bi_5O_7I/PMS displays the optimal degradation of BPAF up to 93.4 % (k_{app} = 0.02984 min^{-1}), which is 5.04 and 3.35 times that of Bi_5O_7I (0.00592 min^{-1}) and MXene/Bi_5O_7I (0.00891 min^{-1}), respectively. However, the degradation rate of the 10-MXene/Bi_5O_7I/PMS system for BPAF decreases to 88.9 %. This is probably because excessive MXene blocks the light and inhibits the photoexcitation of Bi_5O_7I [22]. Notably, the comparison results in Table S2 (Supporting information) demonstrate that the photocatalytic efficiency of the MXene/Bi_5O_7I/PMS system is better than that of various previously reported catalysts.

Fig. 3c shows the influence of the catalyst dosage on the BPAF degradation. The 8-MXene/Bi_5O_7I/PMS system with a catalyst dosage of 0.3 g/L can remove 64.9 % of BPAF in 90 min. As the

dosage of 8-MXene/Bi_5O_7I/PMS is increased to 0.6 g/L, the degradation rate is gradually increased to 93.4%, indicating that the additional reaction sites offered by adequate catalysts can promote the PMS activation and reactive species production. In Fig. 3d, the BPAF degradation rate rises from 79.2% to 93.4% as the PMS concentration increases from 1.00 to 2.00 mmol/L. Nevertheless, the degradation rate decreases when the PMS concentration is further increased to 2.50 mmol/L. Therefore, PMS concentration is positively correlated with the reaction efficiency within the appropriate range, whereas excessive PMS concentration reduces the efficiency because of reactant self-quenching (Eqs. 1–4) [24,25]. Herein, 0.6 g/L 8-MXene/Bi_5O_7I and 2.00 mmol/L PMS are chosen for BPAF degradation.

$$HSO_5^- + {}^{\bullet}OH \rightarrow SO_5^{\bullet-} + H_2O \quad (1)$$

$$HSO_5^- + SO_4^{\bullet-} \rightarrow SO_5^{\bullet-} + SO_4^{2-} + H^+ \quad (2)$$

$$SO_4^{\bullet-} + {}^{\bullet}OH \rightarrow HSO_4^- + 1/2\ O_2 \quad (3)$$

$$SO_4^{\bullet-} + SO_4^{\bullet-} \rightarrow S_2O_8^{2-} \quad (4)$$

The influence of pH on the catalytic activity of 8-MXene/Bi_5O_7I/PMS is explored. In Fig. 3e, 8-MXene/Bi_5O_7I/PMS exhibits excellent catalytic efficiencies over the wide pH range, with corresponding BPAF degradation rates of 88.4%, 90.4%, 94.1%, 94.2% and 94.4%, respectively. Obviously, the photodegradation efficiency increases with the increase of pH. The strong interaction between H^+ and HSO_5^- under acidic conditions probably inhibits the reaction process. Moreover, excessive H^+ can deplete $^{\bullet}OH$ and $SO_4^{\bullet-}$, causing decreased reaction efficiency (Eqs. 5 and 6) [26]. In an alkaline environment, the catalytic performance is improved and even better than that in a neutral environment. This may be because excess H^+ depletes free radicals, and therefore more free radicals are available in alkaline solutions, resulting in greater reaction efficiency.

$$H^+ + {}^{\bullet}OH + e^- \rightarrow H_2O^{\bullet} \quad (5)$$

$$SO_4^- + H^+ + e^- \rightarrow HSO_4^{\bullet-} \quad (6)$$

Photocatalytic stability is critical for the catalytic system. After five cyclic degradation experiments, 8-MXene/Bi_5O_7I/PMS still maintains high activity for degrading BPAF (Fig. 3f). Further characterization by XRD (Fig. S6a in Supporting information), scanning electron microscope (SEM) (Fig. S6b in Supporting information), and TEM (Fig. S6c in Supporting information) reveals that 8-MXene/Bi_5O_7I retains its original crystal structure and morphology, indicating the excellent stability of 8-MXene/Bi_5O_7I.

Electron spin resonance (ESR) tests were utilized to confirm the active species. In Fig. S7a (Supporting information), the strong signal with an intensity ratio of 1:2:1:2:1:2:1 in the 8-MXene/Bi_5O_7I/PMS can be attributed to DMPO oxidation (DMPOX), while the DMPO-$^{\bullet}OH$ and DMPO- $SO_4^{\bullet-}$ signals are not observed. Notably, DMPOX is generated by a second-order reaction of DMPO with an oxidant, implying 8-MXene/Bi_5O_7I rapidly activates PMS and generates numerous oxidized species, indirectly disclosing the existence of $^{\bullet}OH$ and $SO_4^{\bullet-}$ [27]. In Figs. S7b and c (Supporting information), peaks with intensity ratios of 1:1:1:1 and 1:1:1 correspond to $O_2^{\bullet-}$ and $^1O_2$, respectively. Besides, tert–butanol (TBA), methanol (MeOH), L-histidine, and benzoquinone (BQ) were added to perform quenching experiments to further explore the reactive species during the reaction (Fig. S7d in Supporting information). Among them, the addition of L-histidine has the most significant effect on the inhibition of the degradation reaction (23.1% degradation rate), indicating that $^1O_2$ is a key species in the catalytic degradation system.

The light absorption capacity was evaluated by UV–vis diffuse reflectance spectroscopy (DRS) (Fig. S8a in Supporting information). MXene is strongly responsive to light at wavelengths of 250–800 nm, which implies that MXene has metallic properties [28]. Bi_5O_7I has an absorption edge of about 450 nm and exhibits obvious visible light absorption. After the incorporation of MXene, the visible light absorption of MXene/Bi_5O_7I is significantly enhanced. The visible light absorption performance of MXene/Bi_5O_7I increases with the increase of MXene amount. Additionally, the band gap (E_g) of Bi_5O_7I is estimated to be about 2.85 eV based on the Kubelka-Munk equation (Fig. S9a in Supporting information) [29].

Photoelectrochemical measurements were conducted to explore the carrier transport and separation performance of the catalytic materials [30]. Photoluminescence spectra (PL, Fig. S8b in Supporting information) show that the signal intensity of 8-MXene/Bi_5O_7I is the lowest, indicating that it has the best photogenerated carrier separation performance. In the photocurrent response experiment (Fig. S8c in Supporting information), the photocurrent intensity of 8-MXene/Bi_5O_7I is higher than that of Bi_5O_7I. Furthermore, from electrochemical impedance spectroscopy (EIS) in Fig. S8d (Supporting information), the Nyquist semicircle radius of 8-MXene/Bi_5O_7I is small, suggesting a low resistance to carrier transport. These experimental results confirm the higher photoelectron separation efficiency of 8-MXene/Bi_5O_7I, which is attributed to the presence of the Schottky junction.

DFT was applied to analyze the adsorption abilities of PMS and catalysts. The best adsorption configuration is illustrated in Fig. 4. The adsorption energies (E_{ads}) of Bi_5O_7I/PMS (Fig. 4a), MXene/PMS (Fig. 4b), and MXene/Bi_5O_7I/PMS (Fig. 4c) are −0.73, −4.40, and −4.41 eV, respectively, revealing that the adsorption between PMS and catalysts is spontaneous [31]. The E_{ads} increases after the complexation of Bi_5O_7I with MXene, demonstrating that PMS is more easily adsorbed on the surface of MXene/Bi_5O_7I. Moreover, the bond lengths of O–O bonds in free PMS are 1.41 and 1.43 Å in Bi_5O_7I/PMS and MXene/PMS, respectively, whereas the bond length of O–O bonds in MXene/Bi_5O_7I/PMS increases significantly to 1.49 Å, indicating that the activation of PMS by MXene/Bi_5O_7I is stronger.

As shown in Fig. S9b, the Mott-Schottky plot confirms that the flat band potential (E_{fb}) of Bi_5O_7I is −0.53 V *versus* Ag/AgCl, which is further converted to −0.33 V/NHE. For many n-type semiconductors, the E_{fb} is closely related to the conduction band (CB) and is deemed to be more positive by about 0.1 V than its conduction band potentials (E_{CB}). Therefore, the E_{CB} of Bi_5O_7I is calculated to be about −0.43 V/NHE (−4.07 eV/AVS). Since the E_g of Bi_5O_7I is 2.85 eV (Fig. S9a), the E_{VB} of Bi_5O_7I is 2.42 V/NHE (−6.92 eV/AVS) (Fig. 2c). Based on the above analysis, a possible mechanism for the degradation of BPAF by the MXene/Bi_5O_7I/PMS system under visible light is proposed (Fig. 4d). BPAF is efficiently degraded mainly due to the formation of Schottky heterojunction and the synergy between PMS activation and photocatalysis. First, the Schottky barrier in the Schottky heterojunction formed by MXene and Bi_5O_7I (Fig. 2c) inhibits electron-hole complexation and promotes the photocatalysis reaction to proceed. Second, Bi_5O_7I is photoexcited, generating electrons and holes in its conduction and valence bands, respectively (Eq. 7). Due to the Schottky barrier energy, the photogenerated electrons can be efficiently transported to the MXene, thus realizing the fast separation of photogenerated electrons and holes. The electrons can react with oxygen molecules to form $O_2^{\bullet-}$ (Eq. 8) and with PMS to form $SO_4^{\bullet-}$ and $^{\bullet}OH$ (Eqs. 9 and 10), while h^+ reacts with PMS to obtain $SO_5^{\bullet-}$ (Eq. 11) [32]. As exhibited in Eqs. 12 and 13, $SO_5^{\bullet-}$ further reacts with H_2O to generate a large amount of $^1O_2$, in agreement with the ESR test (Fig. S7c) and the quenching experiment (Fig. S7d). Finally, under light-assisted PMS activation, a large amount of ROS is generated to react with BPAF in solution, resulting in efficient degradation of BPAF (Eq. 14).

$$\text{Catalyst} + \text{Visible Light} \rightarrow h^+ + e^- \quad (7)$$

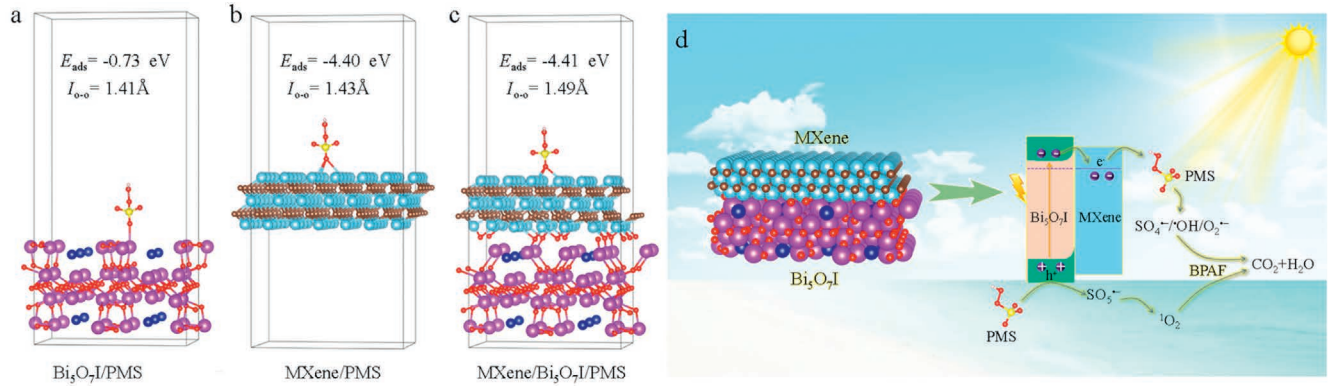


Fig. 4. Optimal adsorption configurations of (a) Bi_5O_7I/PMS, (b) MXene/PMS, and (c) MXene/Bi_5O_7I/PMS systems. (d) Possible mechanism of BPAF degradation in the MXene/Bi_5O_7I/PMS system.

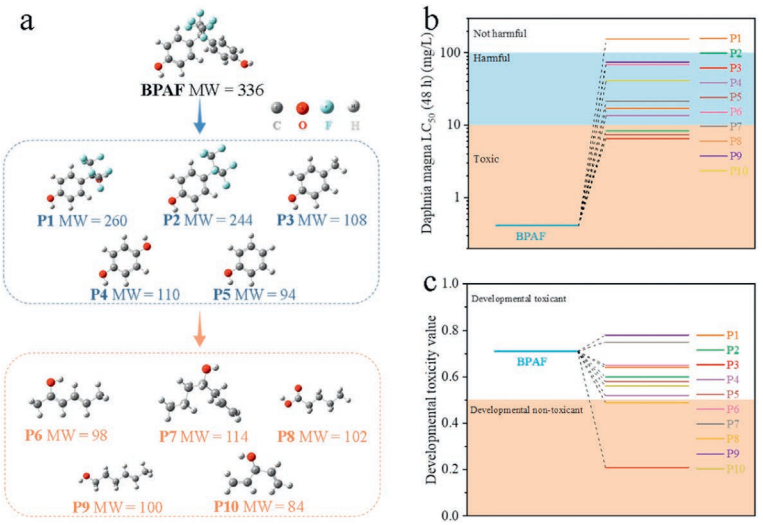


Fig. 5. (a) Proposed photocatalytic degradation pathway of BPAF. (b) Acute toxicity and (c) developmental toxicity of BPAF and its degradation intermediates.

$$e^- + O_2 \rightarrow O_2^{\bullet-} \quad (8)$$

$$e^- + HSO_5^- \rightarrow SO_4^{2-} + {}^{\bullet}OH \quad (9)$$

$$e^{-+}HSO_5^- \rightarrow SO_4^{\bullet-} + OH^- \quad (10)$$

$$h^+ + HSO_5^- \rightarrow SO_5^{\bullet-} + H^+ \quad (11)$$

$$2\ SO_5^{\bullet-} + H_2O \rightarrow 1.5\,{}^1O_2 + 2\ HSO_4^- \quad (12)$$

$$SO_5^{\bullet-} + SO_5^{\bullet-} \rightarrow {}^1O_2 + 2\ SO_4^{2-} \quad (13)$$

$$SO_4^{\bullet-}/{}^{\bullet}OH/O_2^{\bullet-}/{}^1O_2 + BPAF \rightarrow \text{degradation product} \quad (14)$$

To explore the BPAF degradation in the MXene/Bi_5O_7I/PMS system, an in-depth study of the intermediates during the reaction process is required. Therefore, the highest occupied molecular orbital (HOMO), the lowest unoccupied molecular orbital (LUMO), the natural population analysis (NPA), and the Fukui index of BPAF are calculated using DFT to investigate the molecular structural properties and reactive groups that may affect the degradation process of BPAF. Based on the frontier molecular orbital theory, the calculated HOMO (Fig. S10a in Supporting information) indicates that the HOMO of BPAF is mainly located on the phenolic hydroxyl group and the benzene ring, which are susceptible to electrophilic attack by electrophilic oxidizing agents ($^1O_2$) [33]. Meanwhile, the antibonding orbital of LUMO mainly occupies the benzene ring with moderate diffusion to the phenolic hydroxyl group and trifluoromethyl group. The electrostatic potential (ESP) map of the BPAF molecule (Fig. S10b in Supporting information) also reveals that the phenolic hydroxyl group has a partially surface negatively charged region, while the positive charge is mainly concentrated on some of the carbon atoms in the benzene ring.

The concentrated Fukui index (Fig. S10c in Supporting information) is calculated to better characterize the oxidizing capacity of each atom of BPAF. Generally, the Fukui indices f^0 and f^- can represent the atomic radical attack site and electrophilic attack site of BPAF, respectively. The f^0 values of C (1), C (19), C (3), C (17), O (30), and O (32) are 0.0791, 0.0791, 0.0536, 0.0536, 0.0530, and 0.0530, respectively, which make these atoms susceptible to free radical attack. Meanwhile, the f^- values of C (1) (0.0927), C (19) (0.0927), C (4) (0.0821), C (15) (0.0821), C (3) (0.0795), and C (17) (0.0794) are relatively high, indicating that the electrophilic attack induced by $^1O_2$ often occurs around the above atoms.

Moreover, the main intermediates for the degradation of BPAF were ascertained by GC–MS (Table S3 in Supporting information). Ten intermediates are identified and a possible degradation pathway for BPAF is proposed according to product analyses and previous research (Fig. 5a) [34,35]. The pathway consists mainly of (i) an attack of the carbon atoms connecting the two aromatic rings to form **P1** and **P2**, followed by the removal of the fluorine atom to form **P3**, **P4**, and **P5**, and (ii) an attack of the carbon atoms on the aromatic ring leading to a series of ring-opening products (**P6**, **P7**, **P8**, **P9**, and **P10**).

The acute toxicity (*Daphnia magna* LC_{50}, 48 h) and developmental toxicity of intermediates are predicted through the quantitative structure-activity relationship (QSAR) method employing T.E.S.T.

software [36]. In Fig. 5b, the LC_{50} of BPAF for *Daphnia magna* is 0.41 mg/L, which is "Toxic". The degradation intermediates are all less toxic than BPAF. Moreover, the developmental toxicity (Fig. 5c) of all intermediates is lower than that of BPAF (0.71), except for intermediates **P7** (0.75) and **P9** (0.78). This indicates that the catalytic system greatly reduces the BPAF toxicity.

In conclusion, a novel 2D MXene/1D Bi_5O_7I Schottky junction was successfully synthesized for the degradation of BPAF by a PMS-assisted photocatalytic system. The 8-MXene/Bi_5O_7I/PMS system degraded 93.4 % of BPAF within 90 min, which was significantly better than each single component. The introduced MXene not only raised the active sites of the system but also formed 2D/1D microstructures and Schottky structures, which facilitated the interfacial charge transport of the heterojunction and could hinder the photogenerated electron-hole complex. The catalytic mechanism was revealed through a series of DFT calculations combined with experiments. These improved properties and the synergy between photocatalysis and PMS activation enhanced the catalytic performance of the system. This study demonstrated that PMS activation synergized with Schottky heterojunction photocatalysis could efficiently degrade BPAF, which provided new insights into the treatment of organic pollutants.

CRediT authorship contribution statement

Feihu Mu: Investigation, Conceptualization. **Benlin Dai:** Software, Data curation. **Chuxuan Dai:** Investigation, Data curation. **Xiaozhong Chu:** Validation, Methodology. **Jiming Xu:** Validation, Software. **Junyu Shen:** Writing – original draft, Resources. **Wei Zhao:** Software, Methodology. **Guohui Dong:** Writing – review & editing, Visualization.

Declaration of competing interest

The authors declare that they have no known competing financial interests or personal relationships that could have appeared to influence the work reported in this paper.

Acknowledgments

We greatly acknowledge the National Natural Science Foundation of China (No. 22472011), the Natural Science Major Foundation of the Jiangsu Higher Education Institutions of China (No. 22KJA610002), and the foundation of Anhui Province Key Laboratory of Pollutant Sensitive Materials and Environmental Remediation (No. PSMER2023011).

Supplementary materials

Supplementary material associated with this article can be found, in the online version, at doi:10.1016/j.cclet.2025.111866.

References

[1] D. Azizi, A. Arif, D. Blair, et al., Environ. Res. 207 (2022) 112196.
[2] U. Rajamani, A.R. Gross, C. Ocampo, et al., Nat. Commun. 8 (2017) 219.
[3] Y. Hu, Q. Zhu, X. Yan, et al., Environ. Res. 178 (2019) 108732.
[4] J. Moreman, O. Lee, M. Trznadel, et al., Environ. Sci. Technol. 51 (2017) 12796–12805.
[5] N. Liu, N. Lu, H. Yu, et al., Chem. Eng. J. 407 (2021) 127228.
[6] S. Wang, M.R. Razanajatovo, X. Du, et al., Chin. Chem. Lett. 35 (2024) 109140.
[7] D.A. Oluwasogo, S. Varangane, Y.T. Prabhu, et al., J. Cleaner Prod. 394 (2023) 136393.
[8] F. Mu, B. Dai, W. Zhao, et al., Chin. Chem. Lett. 31 (2020) 1773–1781.
[9] Z. Weng, Y. Lin, B. Han, et al., J. Hazard. Mater. 448 (2023) 130869.
[10] R. Guo, H. Zhang, C. Guo, et al., Chin. Chem. Lett. 35 (2024) 109413.
[11] Q. Geng, H. Xie, Y. He, et al., Appl. Catal. B: Environ. 297 (2021) 120492.
[12] F. Mu, B. Dai, W. Zhao, et al., Chin. Chem. Lett. 32 (2021) 2539–2543.
[13] C. Liu, H. Huang, X. Du, et al., J. Phys. Chem. C 119 (2015) 17156–17165.
[14] Z. Li, H. Dong, Z. Wu, et al., Appl. Surf. Sci. 529 (2020) 147162.
[15] J. Wang, C. Cao, Y. Wang, et al., Chem. Eng. J. 391 (2020) 123530.
[16] M. Naguib, M. Kurtoglu, V. Presser, et al., Adv. Mater. 23 (2011) 4207-4207.
[17] J. Li, X. Chen, X. Zhu, et al., Chin. Chem. Lett. 35 (2024) 108286.
[18] A. Sherryna, M. Tahir, ACS Appl. Energy Mater. 4 (2021) 11982–12006.
[19] Z. Zhang, J.T. Yates, Chem. Rev. 112 (2012) 5520–5551.
[20] H. Wu, M. Wang, F. Jing, et al., Chin. Chem. Lett. 33 (2022) 1983–1987.
[21] Q. Liu, Y. Lu, S. Lin, et al., Colloid. Surf. A 594 (2020) 124642.
[22] S. Cao, B. Shen, T. Tong, et al., Adv. Funct. Mater. 28 (2018) 1800136.
[23] G. Zuo, Y. Wang, W.L. Teo, et al., Chem. Eng. J. 403 (2021) 126328.
[24] Q. Hou, M. Wang, T. Li, et al., Chem. Eng. J. 464 (2023) 142566.
[25] Y. Gong, Y. Ding, Q. Tang, et al., Chin. Chem. Lett. 35 (2024) 108475.
[26] J. Lim, D.Y. Kwak, F. Sieland, et al., Appl. Catal. B: Environ. 225 (2018) 406–414.
[27] H. Li, Y. Yao, J. Zhang, et al., Chem. Eng. J. 397 (2020) 125401.
[28] K. Zhang, D. Li, H. Cao, et al., Chem. Eng. J. 424 (2021) 130340.
[29] F. Mu, Q. Cai, H. Hu, et al., Chem. Eng. J. 384 (2020) 123352.
[30] F. Mu, B. Dai, W. Zhao, et al., J. Mater. Sci. Technol. 101 (2022) 37–48.
[31] J. Zhou, X. Guo, X. Zhou, et al., Chem. Eng. J. 433 (2022) 134511.
[32] Q. Wang, Z. Xu, Y. Cao, et al., Chem. Eng. J. 427 (2022) 131953.
[33] W. Li, Y. Zhang, X. Cheng, et al., Sep. Purif. Technol. 282 (2022) 119967.
[34] J. Jia, D. Liu, Q. Wang, et al., J. Hazard. Mater. 424 (2022) 127434.
[35] C. Qin, Y. Qi, Q. Zheng, et al., J. Environ. Chem. Eng. 12 (2024) 112456.
[36] J. Wang, M. Yuan, C. Li, et al., J. Colloid Interface Sci. 612 (2022) 536–549.